Supporting Information

Selective Synthesis of Bi$_2$Te$_3$/WS$_2$ Heterostructures with Strong Interlayer Coupling

Ethan Kahn†‡, Michael Lucking⊥, Fu Zhang†‡, Yu Lei§‡, Tomotaroh Granzier-Nakajima§‡, Daniel Grasseschi△, Kory Beach⊥, William Murray‖, Yin-Ting Yeh§, Ana Laura Elias§‡, Zhiwen Liu‖, Humberto Terrones⊥, Mauricio Terrones†‡§#*

†Department of Materials Science and Engineering, ‡Center for 2-Dimensional and Layered Materials, §Department of Physics, ‖Department of Electrical Engineering, #Department of Chemistry, The Pennsylvania State University, University Park, PA 16802, United States
⊥Department of Physics, Applied Physics and Astronomy, Rensselaer Polytechnic Institute, Troy, New York 12180, United States
△Surface Chemistry & Nanomaterials Laboratory , Department of Inorganic Chemistry, Chemistry Institute, Federal University of Rio de Janeiro (UFRJ), 21941-909, Rio de Janeiro, Brazil

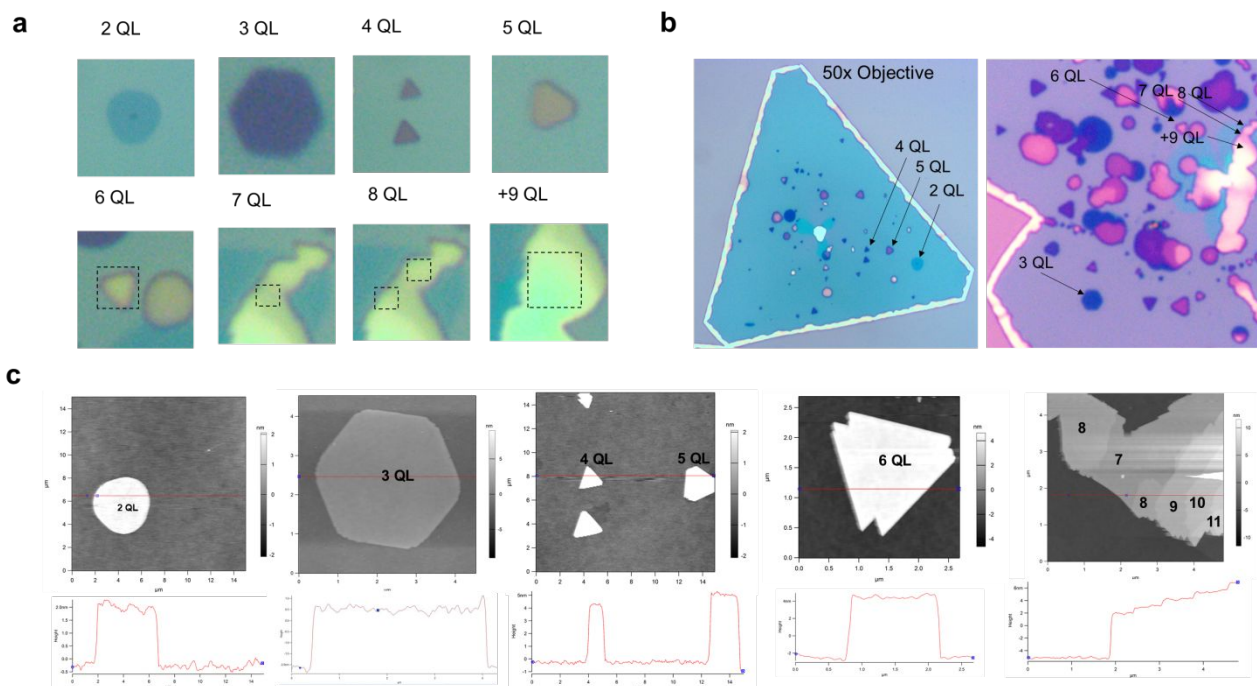Corresponding Author: Mauricio Terrones
Email: mut11@psu.edu

Figure S1. Layer-dependence on VdWH color. (a) Optical micrographs of Bi$_2$Te$_3$/WS$_2$ VdWHs with a 150x objective. (b) Optical micrographs of the same areas at 50x magnification. Note that the color observed depends partly on the optics. For instance, 7-9 layers are difficult to distinguish in (a), but display different shades of pink in the 50x image. (c) AFM data
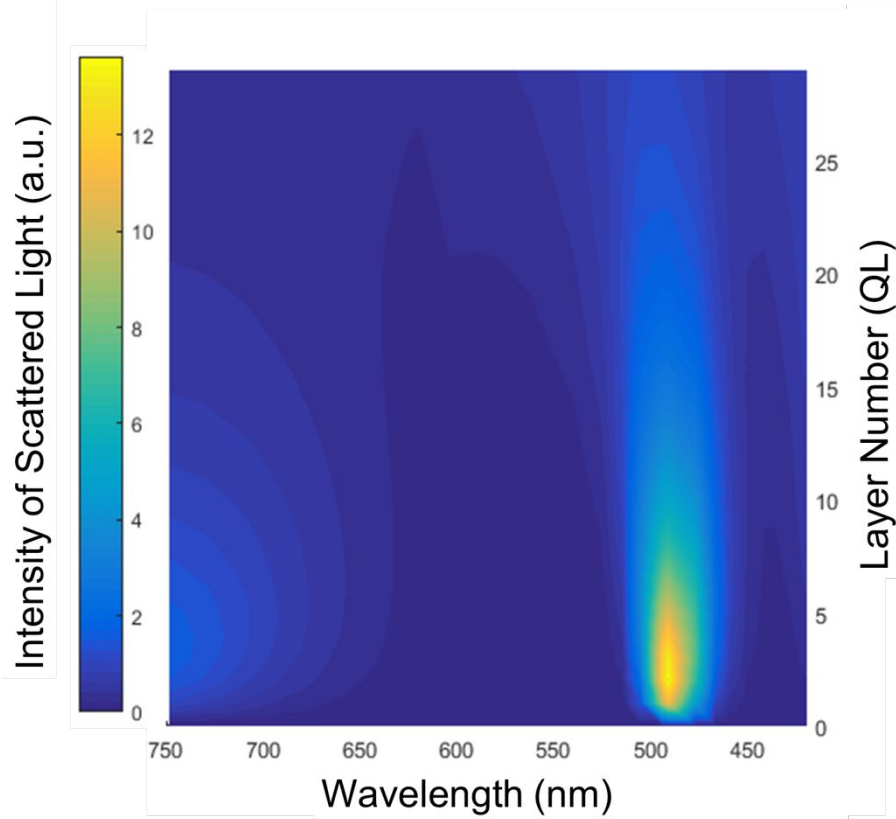
corroborating the layer assignments in (a,b).

Figure S2. Thin film interference calculation. The intensity of backscattering is plotted as a function of layer number and wavelength. Scattering occurs at 4 interfaces: air/Bi$_2$Te$_3$/WS$_2$/SiO$_2$/Si. From known layer thicknesses and dielectric functions,[1–3] the intensity of light backscattered 90° from a thin film may be quantified by

$$I = \int_0^t |F_{ex}(\lambda)F_{sc}(\lambda)|^2 dx,$$

where I is the intensity of backscattered light, t is the thickness of the Bi$_2$Te$_3$, and F_{ex} and F_{sc} represent the effective absorption and backscattering of light from depth x.[4,5] Note that the scattering of green and blue light decreases monotonically with increasing QLs, while that of red light peaks at 5 QL. These trends qualitatively account for the colors we observe, with blue-green (2QL) turning to purple for 3-5 layers, and approaching white for >9QL, as the scattering intensity approaches parity across the visible spectrum.

Creating Defects by Annealing

Annealing at high temperatures is a facile alternative to a plasma treatment for creating defects that does not involve exposure to solvents and polymers, which might alter the 2D material's surface chemistry. Processing parameters including the

temperature, pressure, and the choice of fill gas during annealing will affect the density and identity of the resulting defects. Some mild oxidation likely occurs to the defective crystals, either due to residual oxygen in the reactor, or on exposure to the ambient. Figures SI3,4 illustrate an increase in the nucleation rate of MoS_2 and WS_2 following the creation of defects via annealing.
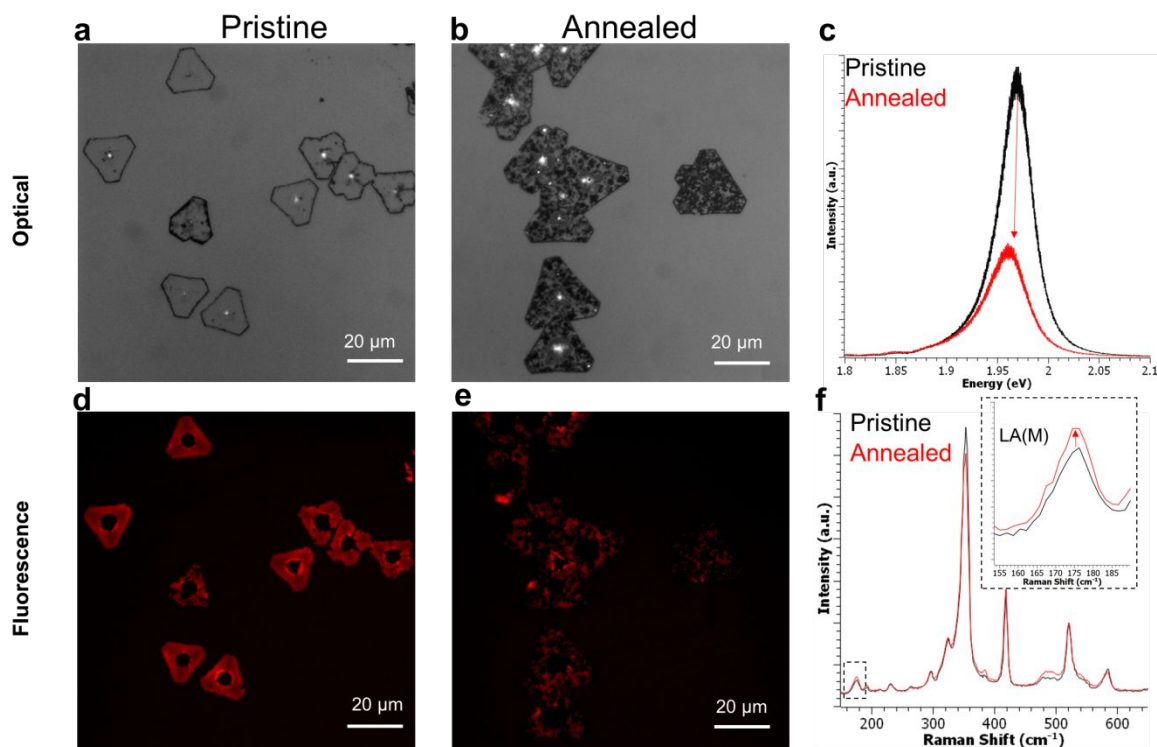

Figure S3. Defect Engineering of Nucleation Density on WS_2. (a,d) Optical and fluorescence images of Bi_2Te_3 grown on pristine WS_2 monolayers. Nucleation is limited to the edges and ad-layers near the crystal's center. (b,e) Optical and fluorescence images of Bi_2Te_3 grown on WS_2 samples annealed under Ar at 50 mTorr and 700 °C for one hour. This process is known to produce 0D defects, primarily sulfur vacancies.[6] On the defective basal plane, the nucleation density is greatly increased. (c) PL spectrum from a WS_2 monolayer before and after annealing. The decreased intensity and broadening of the peak indicate a higher defect density. (f) Raman spectra of WS_2 monolayers with 514nm excitation before and after annealing. An increase in the relative intensity of the LA(M) mode is a signature of defects.[7,8]
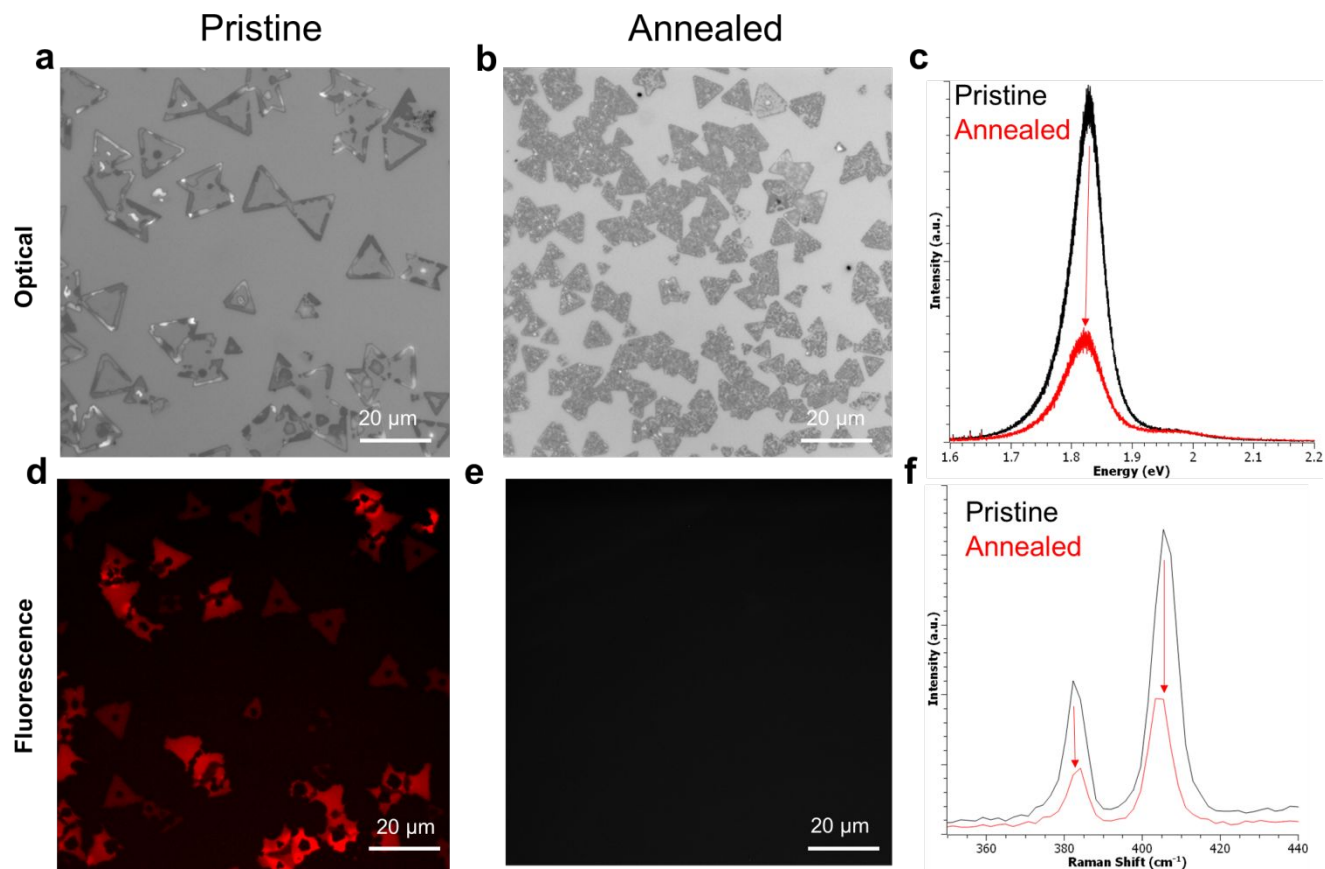
Figure S4. Defect Engineering of Nucleation Density on MoS_2. (a,d) Optical and fluorescence images of Bi_2Te_3 grown on pristine MoS_2 monolayers. Nucleation is limited to the edges and ad-layers near the crystal's center. (b,e) Optical and fluorescence images of Bi_2Te_3 grown on MoS_2 samples annealed under Ar at 50 mTorr and 500 ^{o}C for one hour. (c,f) PL and Raman spectra, respectively, collected with 488nm excitation. Reduced intensities indicate an increase in the defect density.
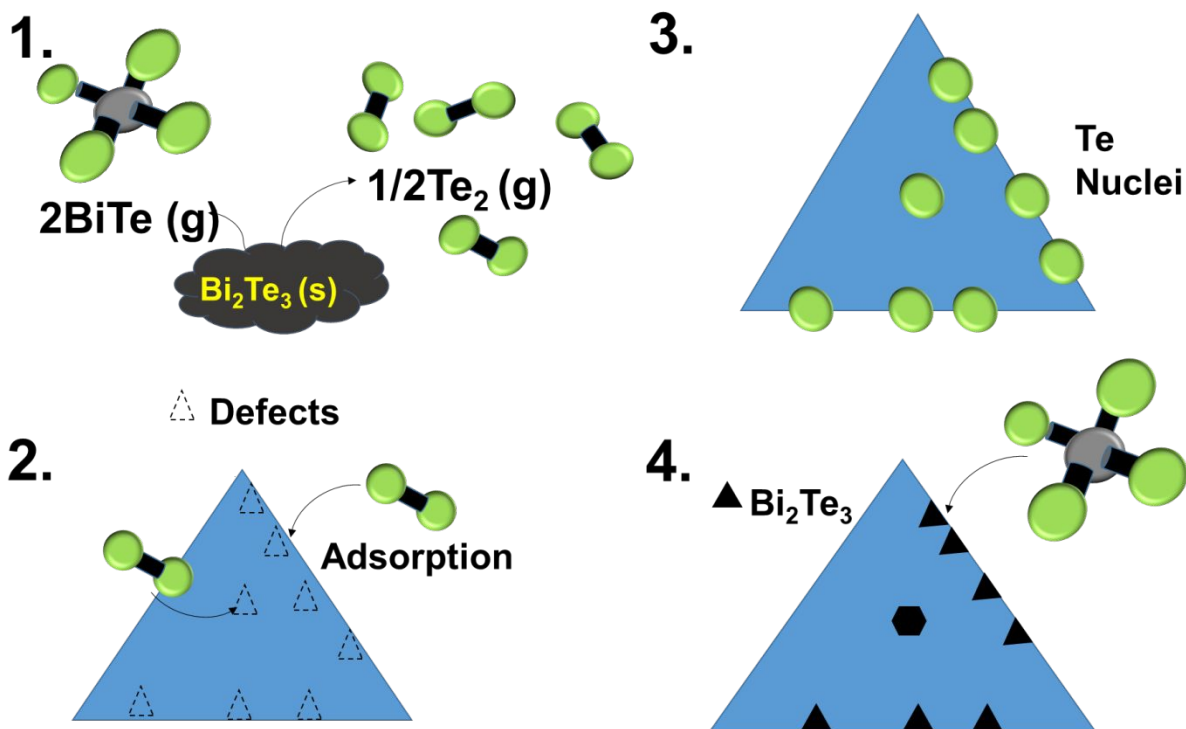
Figure S5. Proposed Mechanism for Enhanced Nucleation. (a) Step 1, vaporization of Bi_2Te_3: For the specific case of Bi_2Te_3, sublimation of the bulk powders is known to proceed incongruently, resulting in a higher partial pressure of Te_2 than BiTe and other Bi-rich phases.[9] Step 2, adsorption of Te_2 on WS_2: As a consequence of this, Te_2 is likely the first compound to deposit on the growth substrate. Step 3, formation of a Te nucleus: it has been observed that PVD growth of Bi_2Te_3 on Si begins with the formation of a Te nucleus, which is stable as a separate phase at typical substrate temperatures.[10] Given the affinity of transition metals for chalcogens, it is plausible that S vacancies and the resulting W dangling bonds play a key role in the adsorption of Te_2, to initiate seed formation. Step 4: Bi_2Te_3 crystal growth. As bismuth-rich species deposit on the substrate, they will grow from Te seeds. A relatively low growth temperature is likely important to the patterned growth seen in the main text. By limiting desorption into the gas phase and surface diffusion away from defective sites, growth can be limited to the patterned regions.

Growth of Te/WS_2 Heterostructures

To test the plausibility of the Te-seeded mechanism outlined in Figure S5, Te/WS_2 vertical heterostructures were synthesized by evaporating Te powders under the same conditions as Bi_2Te_3. Optical micrographs of these heterostructures (Figure S6) indicate nucleation and growth of Te on edges and grain boundaries, similar to the

growth of Bi_2Te_3. This supports the hypothesis that initial deposition of Te in these defect-rich regions seeds the subsequent growth of Bi_2Te_3.
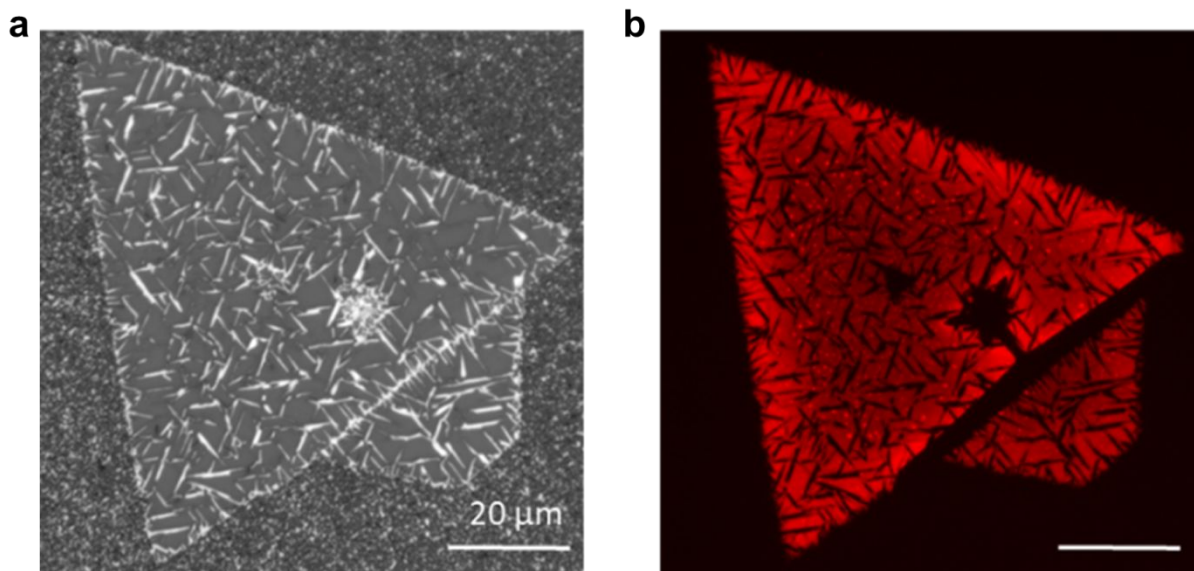

Figure S6. Tellurium nucleation on WS_2. (a) Optical micrograph and (b) fluorescence micrograph of a Te/WS_2 heterostructure. The preferential nucleation and growth of Te on defect-rich edges and grain boundaries indicates the plausibility of a Te-seeded growth mechanism.

Observation of Rod-like Heterostructures

When growth substrates were placed closer to the edge of the furnace, rod-like growth morphologies were also observed. As seen in the optical micrographs of Figure S7, the nucleation of these heterostructures could also be patterned. Because Te grows in rod-like morphologies, further characterization was done to ascertain the identity of these crystals, and gain further insight of the growth mechanism. The TEM displayed in Figure S8 reveals that these rods are made of nanocrystals growing along the zigzag directions of WS_2. Furthermore, the SAED pattern reveals the crystal structure of Bi_2Te_3. While an explanation of this phenomenon is beyond the scope of this work,

these observations suggest that 1D defects or heterogeneities (line defects, wrinkles, etc.) may also play a role in mediating the growth of 2D heterostructures.
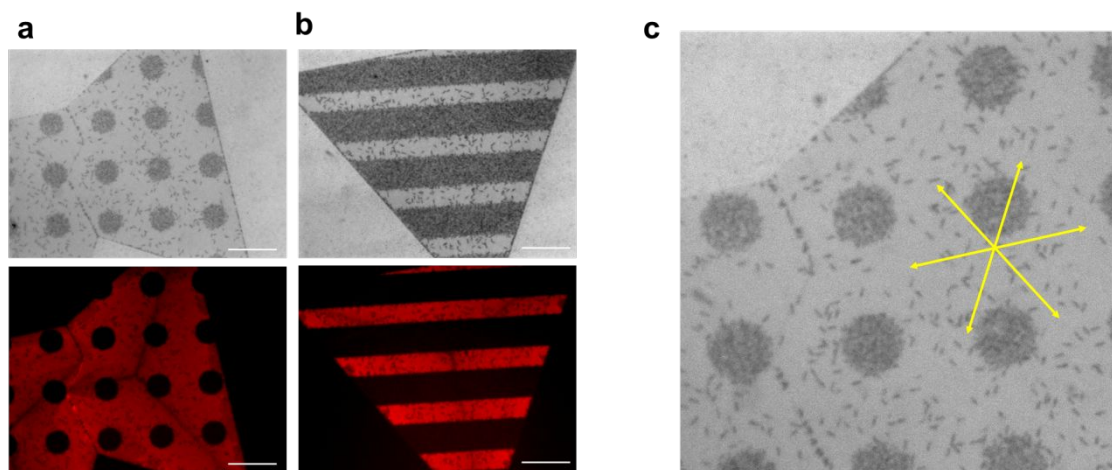

Figure S7. Patterning of rod-like Bi_2Te_3 heterostructures (a,b) Optical and fluorescence images of circle and bar patterns. Scale bars are 20 µm. These structures form when substrates are placed further downstream in the reactor. (c) Higher magnification image of a pattern. Yellow arrows in (c) indicate zigzag directions, with which rods seem to align.
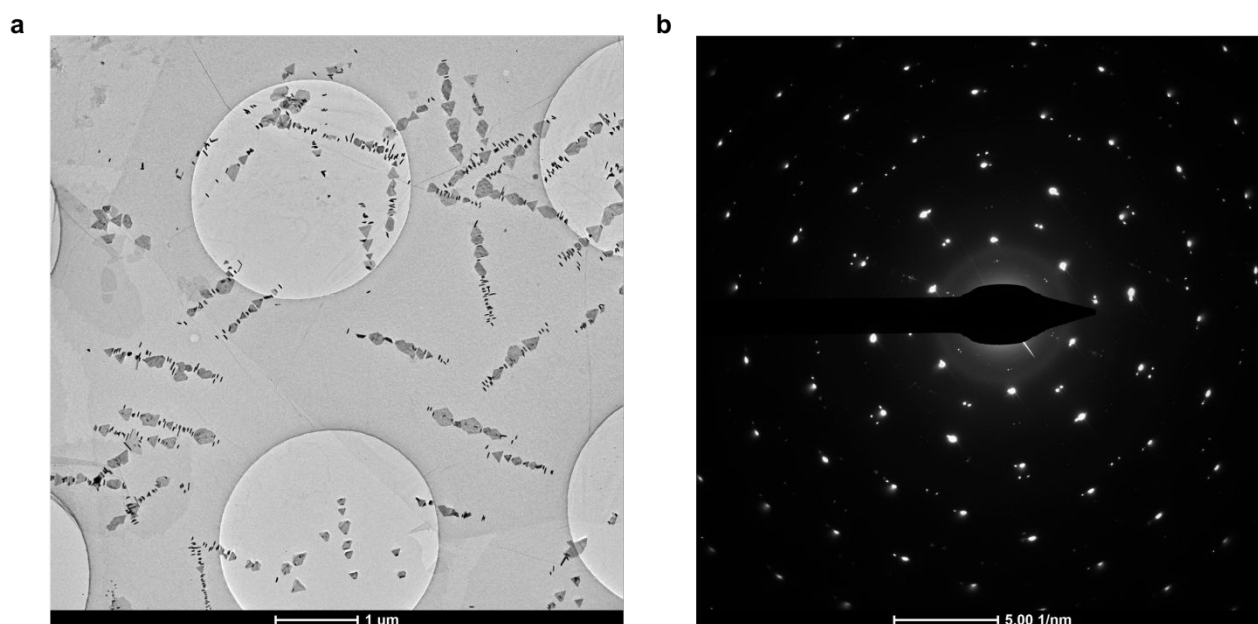

Figure S8. Microscopy of Rod-like Growth. (a) TEM of "rods" indicate that they are actually small 2D layers growing in a line. (b) The SAED pattern reveals that these structures are also Bi_2Te_3. The direction of these rods aligns with zigzag directions, as

indicated in **S5**c. This suggests that 1D defects may also guide the nucleation and growth of Bi_2Te_3 on WS_2.
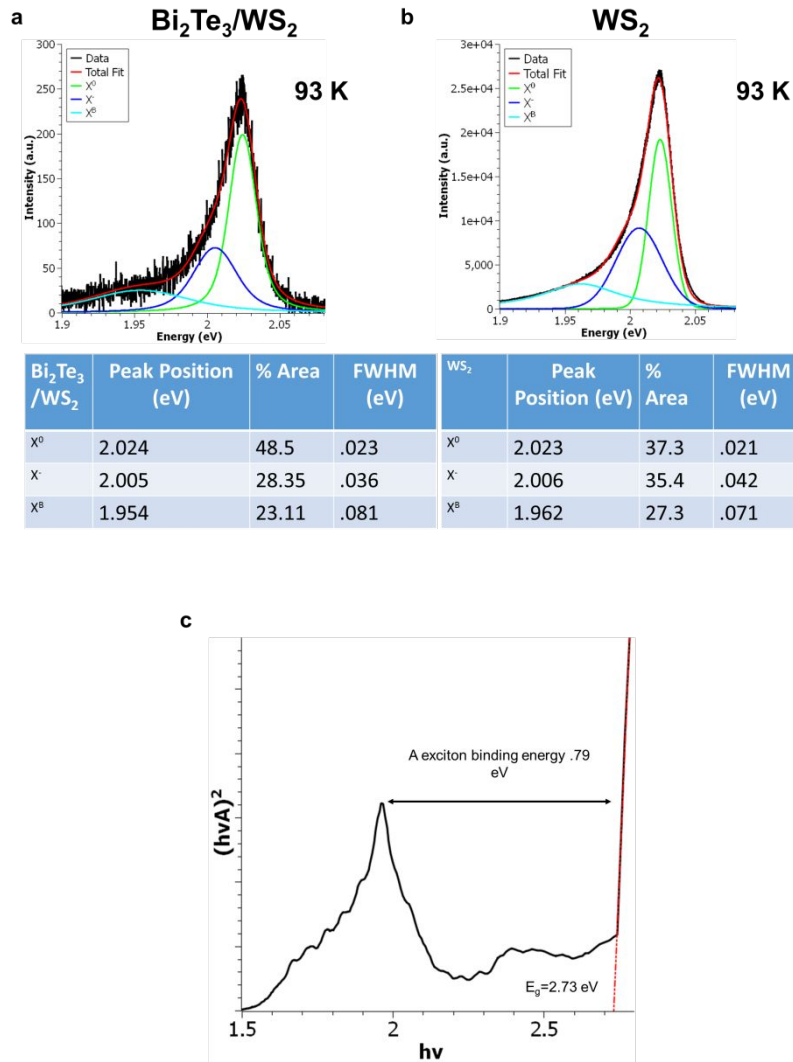

a Bi_2Te_3/WS_2 **b** WS_2

Bi_2Te_3/WS_2	Peak Position (eV)	% Area	FWHM (eV)	WS_2	Peak Position (eV)	% Area	FWHM (eV)
X^0	2.024	48.5	.023	X^0	2.023	37.3	.021
X^-	2.005	28.35	.036	X^-	2.006	35.4	.042
X^B	1.954	23.11	.081	X^B	1.962	27.3	.071

Figure S9. Low Temperature PL and Tauc plot of WS_2 monolayer .(a,b) PL curves from WS_2 and Bi_2Te_3/WS_2 at -180 °C. Neutral exciton (X^0), trion (X^-), and a bound exciton peaks (X^B) are fit. Peak fittings are summarized in the tables below each plot. (c)Tauc plots are a useful way of estimating the band gap of a semiconductor and determining if it is a direct or indirect band gap material, from absorption data.[11] To validate our interpretation of VdWH data, we first measure monolayer WS_2, estimating a quasiparticle band gap of 2.73 eV and an A exciton binding energy of .79 eV. These values are comparable to previous reports.[12]
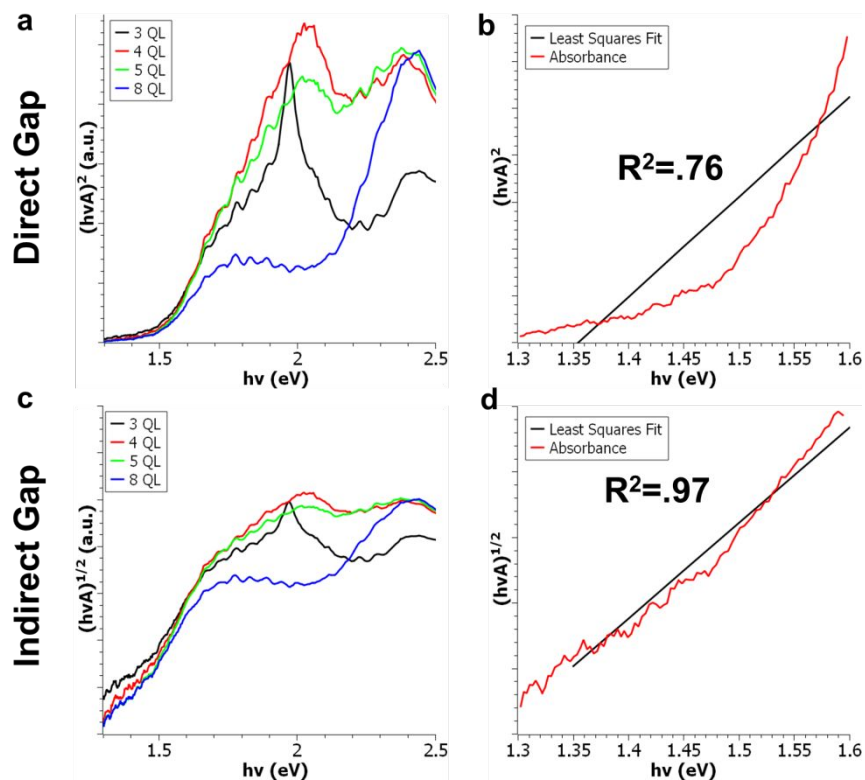
Figure S10. Tauc plots of Bi_2Te_3/WS_2. (a,b) Tauc plots and a representative fitting of the absorption edge, assuming a direct band gap. (c,d) Tauc plots and a representative fitting of the absorption edge, assuming an indirect band gap. These data indicate that the vdWH has an indirect band gap, in agreement with DFT results.
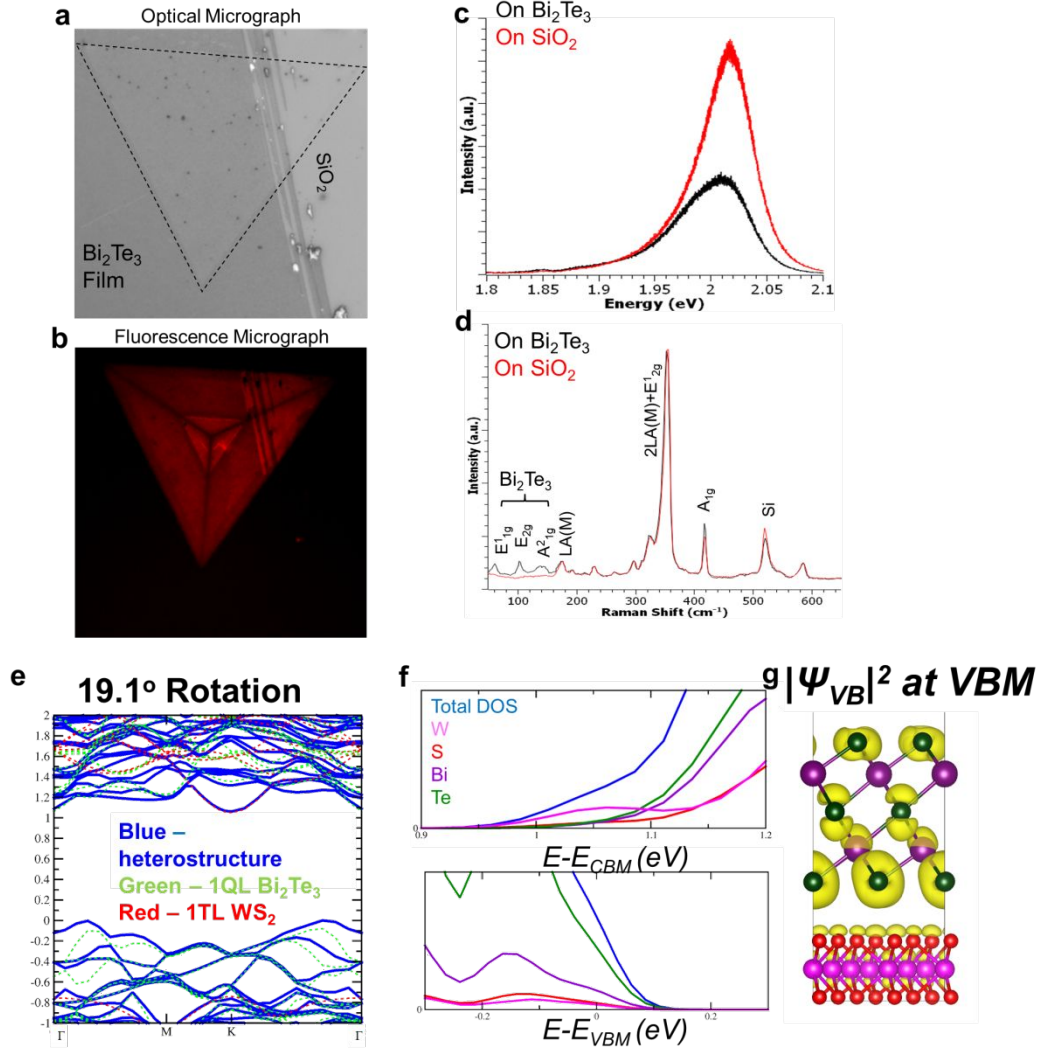
Figure S11. Optical characterization of transferred VdWHs and rotational calculations. (a,b) Optical and fluorescence micrographs of WS_2/Bi_2Te_3 VdWHs formed by the mechanical transfer of WS_2 monolayers onto a scratched, polycrystalline Bi_2Te_3 film with a thickness of 3-4 QL. (c,d) PL and Raman spectra of transferred heterostructures. When compared to of the main text, no signs of strong interlayer coupling are observed (i.e. 99% quenching of PL, decrease in 2LA(M) mode). (e) DFT band structure of 1QL/1TL VdWH with a 19.1° twist. The band structure is qualitatively similar to the epitaxial case. (f) PDOS plot and (g) electron density cloud of the VBM. These figures also indicate orbital contributions to the VBM across the gap for the non-epitaxial case. Consequently, we attribute the poor coupling seen in this figure to the interlayer spacing rather than an arbitrary rotation angle.
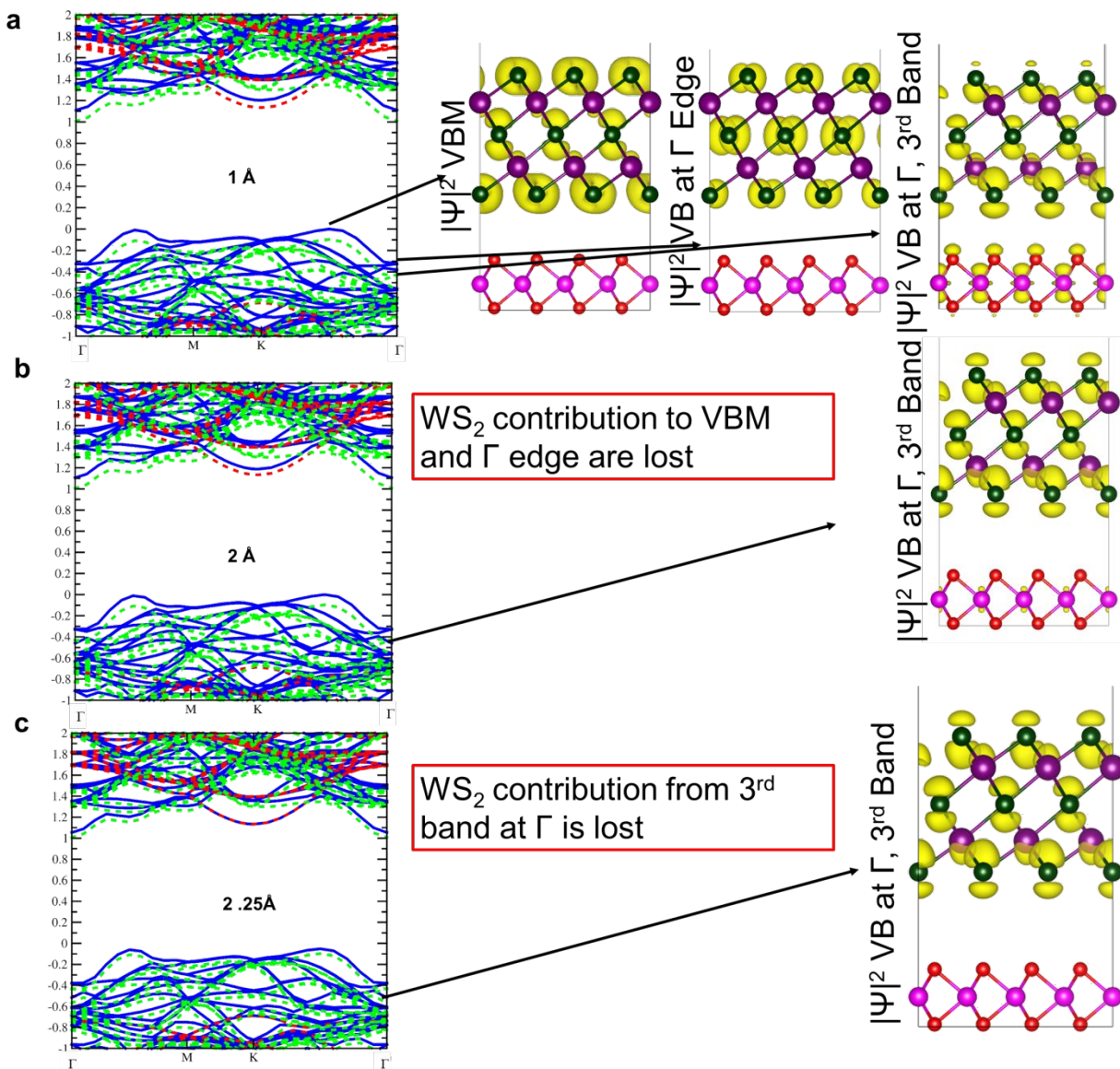
Figure S12. DFT-predicted effects of interlayer spacing. The band structures for spacings of (a) 1 Å, (b) 2 Å, and (c) 2.25 Å are shown with corresponding $|\psi|^2$'s for three positions in the band structure, at the VBM, the valence band edge at the gamma point, and the third highest band at the gamma point, where the WS_2 contribution persists longer. These regions are indicated by arrows on the band structures.

References

(1)   Li, Y.; Chernikov, A.; Zhang, X.; Rigosi, A.; Hill, H. M.; Van Der Zande, A. M.; Chenet, D. A.; Shih, E. M.; Hone, J.; Heinz, T. F. Measurement of the Optical

Dielectric Function of Monolayer Transition-Metal Dichalcogenides: MoS_2, $MoSe_2$, WS_2, and WSe_2. *Phys. Rev. B - Condens. Matter Mater. Phys.* **2014**, *90*, 1–6.

(2)   Aspnes, D. E.; Studna, A. A. Dielectric Functions and Optical Parameters of Si, Ge, GaP, GaAs, GaSb, InP, InAs, and InSb from 1.5 to 6.0 EV. *Phys. Rev. B* **1983**, *27*, 985–1009.

(3)   Cui, H.; Bhat, I.; Venkatasubramanian, R. Optical Constants of Bi_2Te_3 and Sb_2Te_3 Measured Using Spectroscopic Ellipsometry. *J. Electron. Mater.* **1999**, *28*, 1111–1114.

(4)   Li, S. L.; Miyazaki, H.; Song, H.; Kuramochi, H.; Nakaharai, S.; Tsukagoshi, K. Quantitative Raman Spectrum and Reliable Thickness Identification for Atomic Layers on Insulating Substrates. *ACS Nano* **2012**, *6*, 7381–7388.

(5)   Buscema, M.; Steele, G. A.; van der Zant, H. S. J.; Castellanos-Gomez, A. The Effect of the Substrate on the Raman and Photoluminescence Emission of Single-Layer MoS_2. *Nano Res.* **2014**, *7*, 1–11.

(6)   Tongay, S.; Suh, J.; Ataca, C.; Fan, W.; Luce, A.; Kang, J. S.; Liu, J.; Ko, C.; Raghunathanan, R.; Zhou, J.; *et al.* Defects Activated Photoluminescence in Two-Dimensional Semiconductors: Interplay between Bound, Charged and Free Excitons. *Sci. Rep.* **2013**, *3*, 2657.

(7)   Chow, P. K.; Jacobs-Gedrim, R. B.; Gao, J.; Lu, T. M.; Yu, B.; Terrones, H.; Koratkar, N. Defect-Induced Photoluminescence in Monolayer Semiconducting Transition Metal Dichalcogenides. *ACS Nano* **2015**, *9*, 1520–1527.

(8)   McCreary, A.; Berkdemir, A.; Wang, J.; Nguyen, M. A.; Elías, A. L.; Perea-López, N.; Fujisawa, K.; Kabius, B.; Carozo, V.; Cullen, D. A.; *et al.* Distinct Photoluminescence and Raman Spectroscopy Signatures for Identifying Highly Crystalline WS_2 Monolayers Produced by Different Growth Methods. *J. Mater. Res.* **2016**, *31*, 931–944.

(9)   Brebrick, R. F.; Smith, F. T. J. Partial and Total Vapor Pressures over Molten Bi_2Te_3. *J. Electrochem. Soc.* **1971**, *118*, 991.

(10)   Zhao, Y.; de la Mata, M.; Qiu, R. L. J.; Zhang, J.; Wen, X.; Magen, C.; Gao, X. P. A.; Arbiol, J.; Xiong, Q. Te-Seeded Growth of Few-Quintuple Layer Bi_2Te_3 Nanoplates. *Nano Res.* **2014**, *7*, 1243–1253.

(11)   Tauc, J.; Grigorovici, R.; Vancu, A. Optical Properties and Electronic Structure of Amorphous Germanium. *phys. stat. sol.* **1966**, *15*, 627–637.

(12)   Ye, Z.; Cao, T.; O'Brien, K.; Zhu, H.; Yin, X.; Wang, Y.; Louie, S. G.; Zhang, X. Probing Excitonic Dark States in Single-Layer Tungsten Disulfide. *Nature* **2014**, *513*, 214–218.